

Full length article

Five-parameter intervariant boundary characterization of martensite in commercially pure titanium

Ehsan Farabi^a, Peter D. Hodgson^a, Gregory S. Rohrer^b, Hossein Beladi^{a,*}^a Institute for Frontier Materials, Deakin University, Geelong, Victoria, 3216, Australia^b Department of Materials Science and Engineering, Carnegie Mellon University, Pittsburgh, PA 15213-3890, USA

ARTICLE INFO

Article history:

Received 16 February 2018

Received in revised form

9 May 2018

Accepted 10 May 2018

Available online 15 May 2018

Keywords:

Pure titanium

Martensite transformation

Crystallography

Variant selection

Intervariant boundary plane character distribution

ABSTRACT

The intervariant boundary characteristics of a commercially pure Ti microstructure formed by the $\beta \rightarrow \alpha$ martensitic phase transformation were described according to the crystallography of the displacive transformation and the boundary plane orientation. The martensitic transformation created a microstructure whose grain boundary misorientation angle distribution had four distinct peaks that were consistent with the misorientations between the variants produced by the Burgers orientation relationship. Interestingly, about 60% of population corresponded to $60^\circ/[11\bar{2}0]$ intervariant boundaries. Three-variant clusters with a triangular morphology were observed frequently. This configuration is consistent with the phenomenological theory of martensite, which predicts that these clusters, separated by $60^\circ/[11\bar{2}0]$ boundaries, have a lower transformation strain than other possible variant cluster arrangements. Other intervariant boundaries resulted from the impingement of different combinations of distinct three-variant clusters. The five-parameter boundary analysis revealed a strong anisotropy in the plane orientation distribution, showing that boundaries have a tendency to terminate on prismatic $\{hki0\}$ and pyramidal $\{10\bar{1}\}$ planes, when misorientation was ignored. The dominant $60^\circ/[11\bar{2}0]$ intervariant boundaries had symmetric tilt $(\bar{1}101)$ boundary planes, which are a low energy configuration.

© 2018 Acta Materialia Inc. Published by Elsevier Ltd. All rights reserved.

1. Introduction

Grain boundaries have an undisputable effect on the mechanical response of polycrystalline materials. In titanium alloys, grain boundaries impede dislocation motion by imposing barriers that depend on grain boundary type, and this can result in localized stresses [1]. Interestingly, grain boundary geometry and structure affect the localized stress state and the dislocation/grain boundary interaction. Previous studies [2–4] assumed that high angle α/α boundaries in Ti alloys were resistant to dislocation movement and potential sites for cavity nucleation and intergranular fracture. However, the extent of dislocation slip propagation depends on the α boundary characteristics and the type of dislocation. For example, $\{10\bar{1}2\}$ twin boundaries with a low energy configuration [5] impede the prismatic slip dislocations [6], though it can transmit basal dislocations, if the stress is large enough [7–9]. On the other hand, $\{10\bar{1}1\}$ twin boundaries can act as barriers to the basal slip

dislocations [8]. Therefore, by engineering the microstructure and grain boundary network of titanium alloys, it may be possible to optimize the mechanical properties of interest.

Most Ti-alloys undergo the $\beta \rightarrow \alpha$ phase transformation during cooling, which is governed by a specific orientation relationship (OR), known as the Burgers OR [10]. The resultant orientation correspondence between the high temperature β and low temperature α phases provides specific crystallographic α variants, which in return affects the microstructure and texture. Interestingly, the impingement of possible α variants defines specific α/α intervariant boundary arrangements. The formation and arrangement of the variants are influenced by the crystallographic constraints of the transformation, the related transformation strain energy [11–13], and the externally applied strain energy that might arise from deformation or precipitation [14–17].

The strain energy associated with the $\beta \rightarrow \alpha$ martensitic phase transformation stimulates specific α -variant cluster arrangements to accommodate the transformation strain [11,12,18]. These clusters provide a specific population of intervariant boundaries, as indicated by Wang et al. [12] in commercially pure titanium. They have

* Corresponding author.

E-mail address: hossein.beladi@deakin.edu.au (H. Beladi).

shown that the formation of three and/or four α -variant clusters relaxes the transformation strain energy and theoretically results in a high population of $60^\circ/[11\bar{2}0]$ and $63.26^\circ/[\bar{1}0\ 5\ 5\ \bar{3}]$ intervariant boundaries. However, despite the detailed description of the martensitic transformation and the resultant grain boundary network, there is still a lack of information regarding the grain boundary plane character associated with the intervariant boundaries formed in the martensitic microstructure of a commercially pure titanium. A previous study [19] of a Ti-6Al-4V alloy found that the two most common intervariant boundaries have misorientations of $63.26^\circ/[\bar{1}0\ 5\ 5\ \bar{3}]$ and $60^\circ/[11\bar{2}0]$ and have grain boundary plane orientations of $(4\bar{1}\bar{3}0)$ and $(\bar{1}011)$, respectively.

In the current study, commercially pure Ti was subjected to a martensitic transformation and its intervariant boundary plane characteristics were studied using a stereological interpretation of conventional EBSD maps. This five-parameter crystallographic analysis made it possible to measure the grain boundary plane distribution of all intervariant boundaries in the martensitic microstructure [20]. The microstructure characteristics were consistent with the phenomenological theory of martensite, which was used to calculate the transformation strain energy in commercially pure titanium to determine the nucleation possibilities for different α -variant cluster arrangements and the associated intervariant boundaries.

2. Experimental procedure

2.1. Material and heat treatment procedure

The commercially pure titanium used for this study had a grade II chemical composition [21], was received in an extruded condition, and had an equiaxed microstructure. The sample was heat treated in an induction furnace embedded in a servo-testing machine. To prevent the titanium from being oxidized at high temperature, it was coated with glass (a delta glaze coating). The sample was reheated to 950°C and held for 3 min to transform the entire microstructure to the β -phase, before water-quenching it to room temperature, to obtain a martensitic microstructure.

2.2. Microstructural and texture characterization

The microstructure and texture of the samples were studied by scanning electron microscopy (SEM) equipped with electron back-scattered diffraction (EBSD) technique along with transmission electron microscopy (TEM). Note that the microstructure was not uniform through the thickness of 10 mm. At the surface, it was mostly martensitic, but in the middle of the sample, the microstructure was a mixture of martensitic and Widmanstätten α -phase. Because of the low thermal conductivity of Ti alloys ($K = 19 - 23\ \text{W}\cdot\text{m}^{-1}\cdot\text{K}^{-1}$ [22]), it is likely that the cooling rate was slower in the centre of the sample than on the surface. To measure the cooling rate, two holes with 1.1 mm diameter were drilled along the diameter of $10\ \text{mm} \times 15\ \text{mm}$ cylindrical sample at depths of 5 mm (centre) and 9 mm (sub-surface). K-type thermocouples wire were brazed into the holes and temperature profile was recorded throughout the heat treatment schedule for both positions. The heat treatment was conducted 3 times to examine the reproducibility of the result. The measured cooling rates were $135 \pm 15^\circ\text{C/s}$ and $175 \pm 9^\circ\text{C/s}$ at the centre and sub-surface of sample, respectively. Recognizing this gradient, all microstructure and texture measurements were conducted approximately $1000\ \mu\text{m}$ beneath the surface of the water-quenched sample, a region that was close enough to the surface to obtain martensitic microstructure while far enough away not to be affected by oxidation.

EBSD analysis: A two-step procedure was used to prepare the

EBSD samples. First, the samples were ground to 4000 grit SiC paper and then mechanically polished with a $0.4\ \mu\text{m}$ OPS suspension. In the second step, the surface was electro-polished by an appropriate electropolishing routine (i.e., a voltage of 30 kV and at the temperature of 22°C) and the A3 Struers™ electrolyte solution (i.e., 240 ml Butoxyethanol, 400 ml methanol, 40 ml Perchloric acid). The microstructure was then examined by EBSD on a plane parallel to the extrusion direction. The EBSD measurements were conducted using a FEG Quanta 3-D FEI SEM instrument equipped with a fully automated EBSD device. The EBSD measurements were made with an accelerating voltage of 20 kV, a working distance of 10.5 mm, and on a hexagonal grid with a step size of $1\ \mu\text{m}$ (as-received sample) or $0.3\ \mu\text{m}$ (martensite sample). Multiple scans covering an area of $\sim 875,000\ \mu\text{m}^2$ have been measured by EBSD for the martensitic microstructure. The average confidence index was between 0.4 and 0.6. The EBSD post-processing was conducted using the TexSEM Laboratories Inc., software (TSL).

Intervariant boundary analysis: A stereological analysis, which has been described previously [20,23], was used here to identify the intervariant boundary plane distribution in the martensitic structure. This approach was employed extensively in earlier studies for different materials [24–28]. The number of boundary segments/traces required for such a measurement depends on the crystal structure (50,000 segments/traces for cubic and 200,000 for hexagonal materials [20]). Before extracting the boundary segments from the EBSD maps, a multiple step cleaning procedure was conducted. First, the ambiguous data was removed through the grain dilation function. Then, a single average orientation was assigned to the neighbouring groups of pixels with a disorientation angle of less than 5° (one single grain). To extract the boundary line traces/segments from the EBSD data, the reconstructed grain boundary function with a boundary deviation limit of 2 pixels ($0.6\ \mu\text{m}$) [29] was used. Here, a total of $\sim 200,000$ boundary line traces were extracted from the EBSD maps. After extracting the line segments, the stereological procedure was applied to calculate the five-parameter grain boundary character distribution (GBCD). The five-parameter GBCD was then used to determine the grain boundary plane distribution at different grain boundary misorientations.

TEM analysis: To produce TEM foils, discs of 3 mm in diameter were taken from $1000\ \mu\text{m}$ below the surface. They were then mechanically ground to a thickness of $\sim 70\ \mu\text{m}$ and then twin-jet electro-polished using the solution employed for EBSD sample preparation. The electro-polishing was conducted at a temperature of about -40°C and a voltage of 30 V. TEM examination of thin foils was conducted using a JEM 2100 microscope operated at 200 kV.

Texture measurements: The overall texture of the as-received and transformed samples was measured by EBSD using a Zeiss LEO 530 FEG SEM instrument equipped with an Oxford Instruments EBSD attachment. The data were obtained using the Aztec software and processed using the HKL channel 5 software. As discussed later, the parent β phase undergoes significant grain growth during reheating to 950°C . To obtain unbiased and statistically reliable texture data from many grains, the EBSD measurements were carried out using a coarse step size of $30\ \mu\text{m}$ on 30 different sections of both the as-received and martensitic samples, covering an area of $4.17\ \text{mm} \times 3.12\ \text{mm}$.

3. Results

The as-received equiaxed microstructure had an average grain size of $10.9 \pm 0.1\ \mu\text{m}$ (Fig. 1). The overall crystallographic texture of the as-received titanium revealed a strong fibre texture with an intensity of 6.2 multiples of a random distribution (MRD) (Fig. 2a), which is typical for extruded titanium alloys [30]. The intensity of

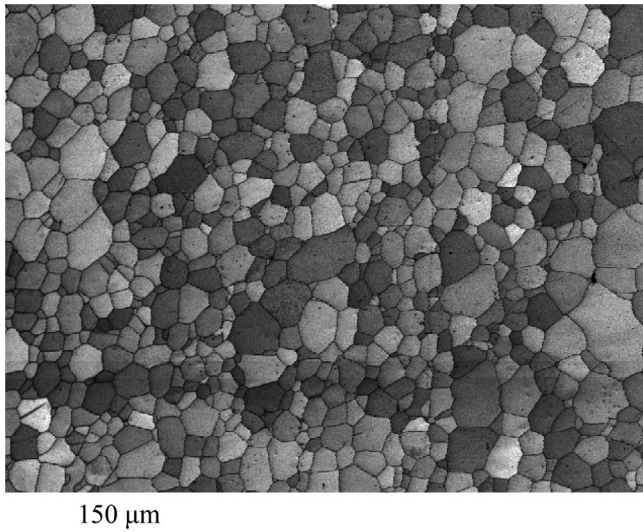


Fig. 1. The band contrast image of the as-extruded commercially pure titanium alloy.

the texture arises from the alignment of the $[0001]$ axes perpendicular to the extrusion direction. The $(1\ 0\ \bar{1}\ 0)$ and $(1\ 1\ \bar{2}\ 0)$ pole figures revealed maxima mainly around extrusion direction with an intensity of 3.5 MRD (Fig. 2a). The main texture component covers about 43.2% of the orientation space.

3.1. The evolution of microstructure and texture in martensite transformation

The data in Fig. 3 show that the heat treatment procedure results in a microstructure that resembles martensite, as fully martensitic microstructure is difficult to form in commercially pure Ti due to the absence of alloying elements. A bright field TEM examination also confirmed the presence of elongated martensitic laths, typically contained only internal dislocations without any transformation twinning (Fig. 4). This structure hereafter is referred to as a martensitic microstructure. The two-dimensional EBSD images showed two distinct morphological features. The first were elongated packets of martensitic laths stacked up in parallel arrays (Fig. 3b–c). The parallel laths were separated either by low misorientation angle boundaries ($\leq 5^\circ$) (Fig. 3b) or by high misorientation angle boundaries, mostly with a misorientation of $60^\circ/[1\ 1\ \bar{2}\ 0]$ (Fig. 3c). The second morphology consisted of the martensitic laths stacked up in a triangular shape (highlighted as 'C' in Fig. 3a). The interior of the triangle was progressively filled with smaller triangles (highlighted as 'D' in Fig. 3a and shown in Fig. 3d). This suggests that the first laths that nucleate fragment the parent β -grain and reduce the volume available for the nucleation of new variants, leading to a smaller average lath size. The variants formed in the triangular morphology were mostly separated by boundaries with a $60^\circ/[1\ 1\ \bar{2}\ 0]$ misorientation (Fig. 3d). It should be noted that the observation of the triangular morphology depends on the orientation of the section plane through the grain.

Interestingly, the texture after the martensitic transformation was nearly the same as the as-received condition (Fig. 2), though the fibre consisted of multiple maxima. In general, the martensitic transformation led to a decrease in the overall texture intensity from 6.2 MRD to 5 MRD for the $\{0001\}$ pole figure (Fig. 2b). Although the $\{10\bar{1}0\}$ and $\{11\bar{2}0\}$ pole figures showed similar overall textures to the as-received condition, their texture strengths were different. The overall texture in the $\{10\bar{1}0\}$ pole figure decreased from 3.5 MRD in the as-received condition to 2.6 MRD

after the martensitic transformation. By contrast, the intensity of the maximum in the $\{11\bar{2}0\}$ pole figure increased from 3.5 MRD to 6 MRD (Fig. 2).

3.2. The martensite intervariant boundary plane character distribution

The misorientation angle distribution of the martensitic microstructure revealed multiple peaks at the positions of $\sim 10^\circ$, $55\text{--}65^\circ$ and $\sim 90^\circ$, which was significantly different from what is expected from a random distribution (Fig. 5a). The misorientation axis distribution associated with each peak was clustered at a specific axis. According to the Burgers orientation relationship, the $\beta \rightarrow \alpha$ phase transformation in titanium can create 12 distinct α -phase variants from a given prior parent β -grain. These variants are listed in Table 1. The impingement of these α -variants establishes 11 intervariant boundaries (Table 1). However, because of crystal symmetry, there are only 5 distinct misorientation angle/axis pairs (Table 1). These intervariant boundaries are consistent with the observed misorientation angle/axis distribution (Fig. 5a), meaning that the martensitic phase transformation closely followed the Burgers orientation relationship. However, the distribution of observed intervariant interfaces differed significantly from those expected in a theoretical distribution calculated under the assumption that all variants occur in the product phase with equal probability (Fig. 5b). Interestingly, the most common intervariant boundary has a misorientation of $60^\circ/[11\bar{2}0]$, and makes up 60% of all boundary length. The $10.53^\circ/[0001]$ intervariant was the least common, making up only 2% of all boundary length. The length fractions of the $60.83^\circ/[\bar{1}.377\ \bar{1}\ 2.377\ 0.359]$, $63.26^\circ/[\bar{1}0\ 5\ 5\ \bar{3}]$ and $90^\circ/[1\ \bar{2}.38\ 1.38\ 0]$ intervariant boundaries were $\sim 12\%$, 13% and 6% , respectively.

The relative areas of all boundary planes, independent of misorientation, are plotted in stereographic projection in the crystal reference frame (Fig. 6). In the distribution, the $\{0001\}$ basal plane is placed in the centre of the stereogram and the prismatic planes ($\{11\bar{2}0\}$ and $\{10\bar{1}0\}$) are located at the circumference of the stereogram. The distribution was anisotropic with a maximum intensity of 1.6 MRD, revealing two characteristic peaks at prismatic and pyramidal orientations. The first peak is positioned at the $\{4\bar{1}\bar{3}0\}$ orientation and spreads towards $\{10\bar{1}0\}$. The second peak corresponds to a pyramidal plane with the $\{10\bar{1}1\}$ orientation. Interestingly, the distribution minimum was positioned at the $\{0001\}$ orientation (Fig. 6).

The maxima in the misorientation angle/axis distribution (Fig. 5a) specify the misorientations where the distribution of grain boundary planes should be examined. Here, the distribution of intervariant boundary planes for each misorientation was plotted in stereographic projection and compared with the schematic representation of the characteristic grain boundaries drawn by the Glowinski's grain boundary toolbox software [31] (Fig. 7). The distribution of grain boundary planes at the $10.53^\circ/[0001]$ misorientation had no maxima greater than 0.5 MRD and was not considered significant. The distribution of intervariant boundary planes for grain boundaries with a misorientation of $60^\circ/[1\ 1\ \bar{2}\ 0]$ had a single maximum near the pyramidal $(\bar{1}101)$ plane with the maximum intensity of 500 MRD (Fig. 7a). The ideal symmetric tilt boundary, which also has 180° -twist and 180° -tilt character, has the $(\bar{1}7\ 17\ 0\ 18)$ orientation. The orientation of the ideal plane differs from $(\bar{1}101)$ by only 1.6° , which is less than the resolution of the distribution, which is about 10° . The boundary plane distribution for the $60.83^\circ/[\bar{1}.377\ \bar{1}\ 2.377\ 0.359]$ intervariant boundary has a maxima near (9630) planes with an intensity of 14 MRD. This boundary was deviated by $\sim 4^\circ$ from the $(\bar{5}320)$ tilt boundary, which is also within the experimental resolution (Fig. 7b). For the $63.26^\circ/$

$[\overline{10}553]$ intervariant boundary, there was a peak around the $(\overline{19}1363)$ plane with a maximum intensity of 200 MRD. This plane is $\sim 6^\circ$ from the $(\overline{3}210)$ twist and 180° -tilt boundary plane (Fig. 7c). The intervariant plane distribution for the $90^\circ/[1\overline{2}3\overline{8}1.380]$ has a diffuse maximum at the $(17\overline{17}018)$ plane with an intensity of 30 MRD. This boundary also has twist and 180° -tilt character, and spreads between the $(1\overline{2}13)$ and $(\overline{4}3\overline{1}0)$ planes (Fig. 7d).

4. Discussion

4.1. Transformation texture and variant selection

The martensite overall texture is qualitatively similar to the overall texture of the extruded sample, revealing a fibre texture with $[0001]$ perpendicular to the extrusion direction (Fig. 2). This is mostly due to the texture memory effect, which was also reported by others when the material was subjected to a heat treatment above the transus temperature through both experiment and simulation in steel [32] and Ti alloys [30,33,34]. The extruded α grains in the as-received microstructure transform to the β parent

during the reheating at 950°C and this transforms back to martensitic α during cooling. The presence of the Burgers OR for both transformations to some extent leads the martensitic transformation texture to be similar to the starting extrusion texture. However, it is worth mentioning that the parent β grains grow during annealing at 950°C , eliminating some pre-existing orientations and resulting in a relatively coarse grained structure before the martensitic transformation on rapid cooling.

Despite the texture similarity, the martensitic transformation produces a weaker overall texture and the appearance of multiple peaks in the (0001) pole figure (Fig. 2). The texture weakening is expected because rapid cooling reduces the difference in the phase transformation driving force for distinct variants, promoting the formation of all possible variants associated with Burgers OR in a given parent β grain (variant multiplication). This ultimately reduces the overall texture strength. However, the presence of multiple peaks suggests that some variant selection does occur in the transformation to accommodate the transformation stress/strain. Variant selection should not promote specific orientation/s because of variant multiplication. On the other hand, the coarsening of the β

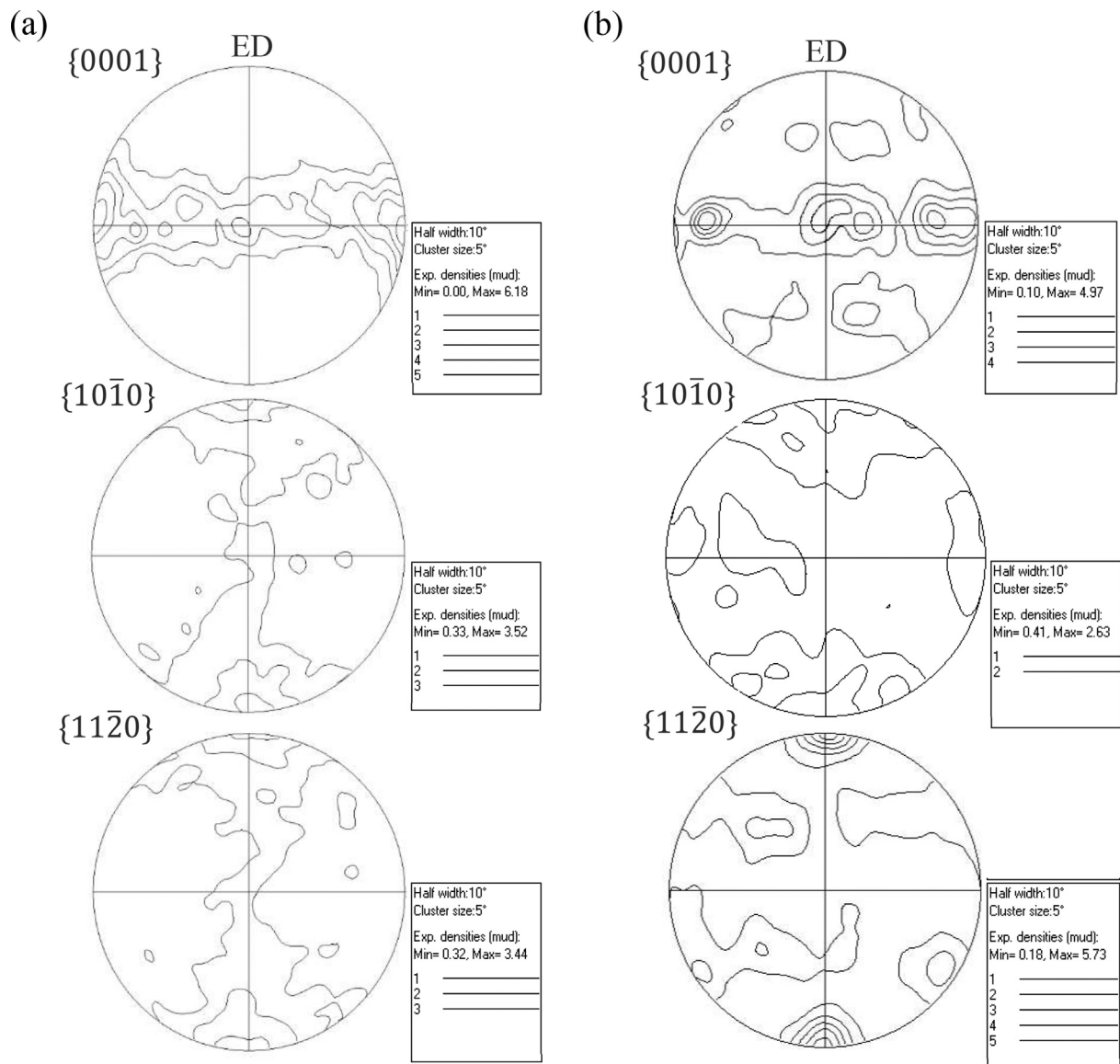


Fig. 2. The basal and prismatic pole figures of (a) the as-extruded and (b) the martensitic microstructures. ED is the extrusion direction.

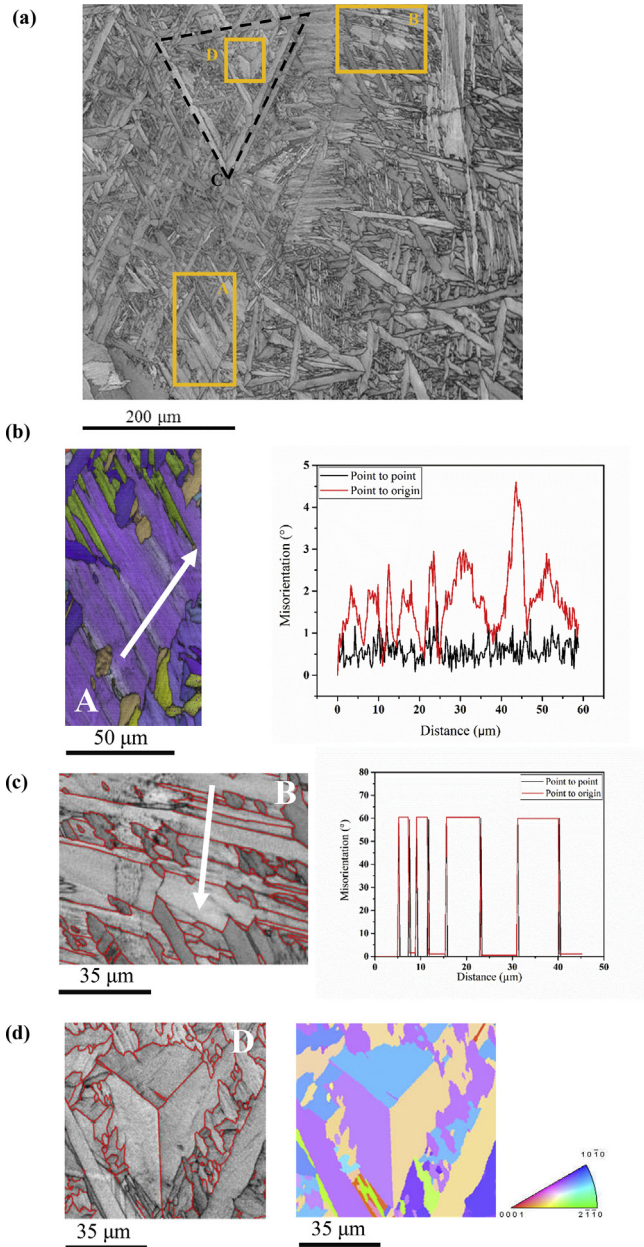


Fig. 3. a) The image quality map of the martensitic microstructure revealing different morphologies; (b) parallel laths separated by low angle boundaries, highlighted by “A” in (a), c) parallel laths separated by the $60^\circ/[11\bar{2}0]$ boundaries, shown by “B” in (a), and d) 3 differently oriented variants clustered in an indentation and/or triangular shape, separated by the $60^\circ/[11\bar{2}0]$ boundaries, marked by “C” in (a). The triangle inset in (d) represents the colour codes referred to normal direction. The red lines indicates the $60^\circ/[11\bar{2}0]$ boundaries in (c) and (d). (For interpretation of the references to colour in this figure legend, the reader is referred to the Web version of this article.)

grains may lead to the strengthening of a specific β orientation and/or the promotion of low energy β grain boundaries [34,35], which may promote a specific α crystallographic variant/orientation on either side of the β -boundary [33,36,37]. A similar observation is made here through back-calculating the orientation of the high temperature parent β phase from martensitic α -variants obeying the Burgers OR (Fig. 8), using the software developed in the Lorraine university, as described in Ref. [38]. It appears that the presence of special β boundaries provides preferred nucleation sites for α variants sharing same Burgers orientation relationship with both β grains (i.e., having similar orientations) at either side of the parent

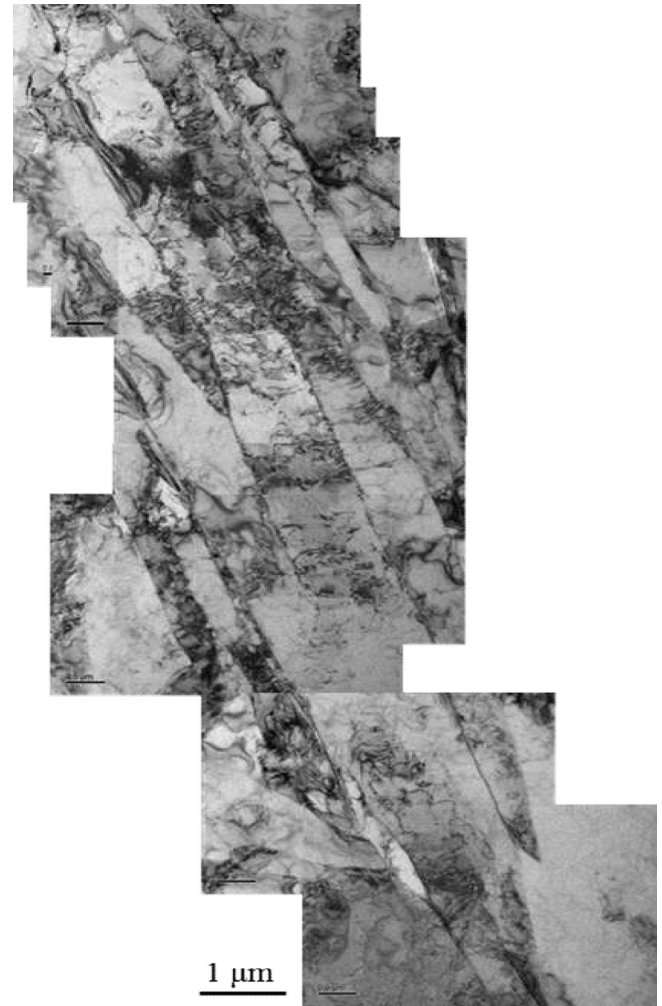


Fig. 4. TEM bright-field micrograph of the martensitic α laths containing dislocation substructure.

β grain boundary (Fig. 8). In other words, the α variants nucleated at either side of the β/β boundary sharing a common $(110)_\beta$ pole have the same (0001) pole and obey Burgers OR with both parent β grains (i.e., double Burgers boundary) [36,39]. Similar observations have been reported after the martensitic transformation of a rolled Zr alloy [40]; limited variant selection on special β -boundaries led to a texture memory effect and the promotion of a specific texture component.

4.2. Rationalization of the martensitic microstructure in pure titanium

The martensitic transformation in materials usually results in a relatively large shape change, which is accommodated by specific variant arrangement/s to minimise the associated strain energy. In the case of commercially pure Ti, where the martensite transition temperature is as high as $802 \pm 10^\circ\text{C}$, the shape change can be accommodated by the plastic flow of the relatively soft matrix. In the current study, the martensitic laths have a wedge shaped morphology, assembled into triangular clusters of three differently oriented variants (Fig. 3). This is a common characteristic of the self-accommodation morphology. Interestingly, there were no signs of twins inside the assembled laths (Fig. 3), suggesting that slip is the dominant operating mode for accommodation of

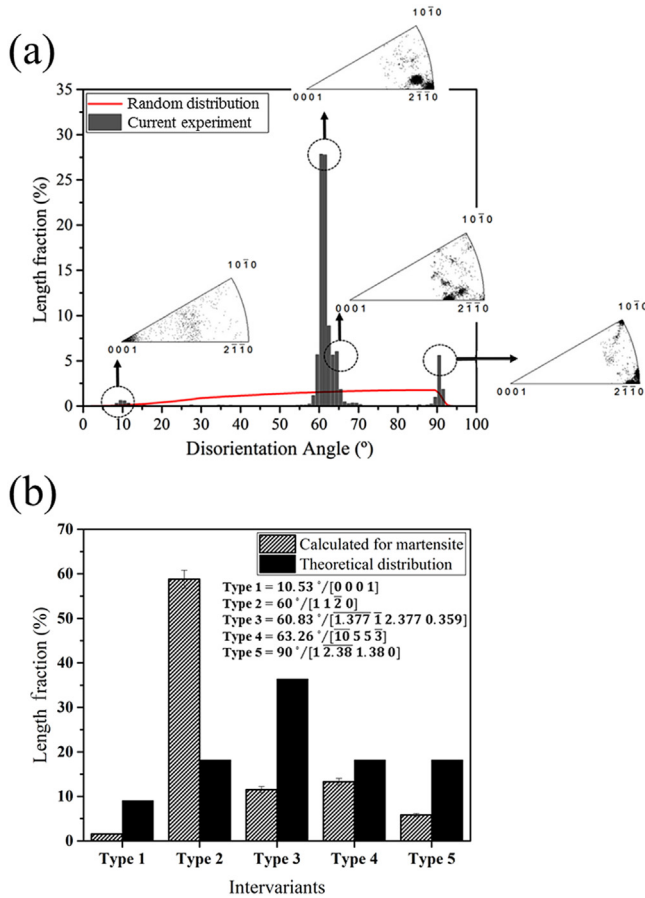


Fig. 5. a) The misorientation angle distribution of martensitic microstructure of CP titanium alloy, and b) the length fraction of intervariant boundaries associated with Burgers orientation relationship. The theoretically calculated fractions are based on the assumption that all variants have equal statistical probability during the phase transformation.

inhomogeneous strain at high temperatures. This implies that the critical resolved shear stress for slip is less than for twinning at the transformation temperature [41]. The clustering of the martensite variants to minimise the transformation induced shear strain is known as the self-accommodation phenomenon [42], which influences characteristics of the microstructure including the texture and the intervariant boundary characteristics. To test the idea that these clusters do minimise the transformation strain, the

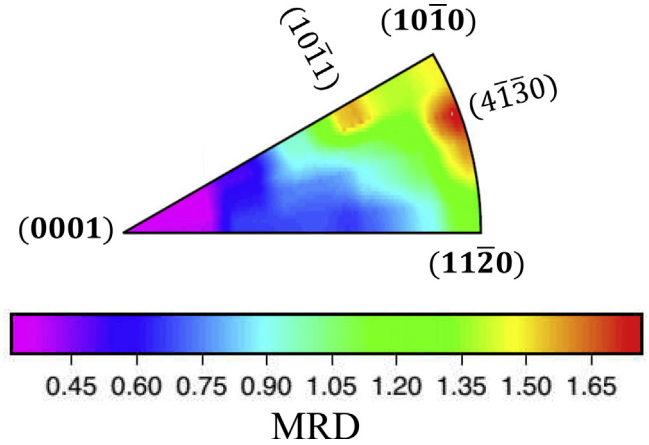


Fig. 6. The distribution of grain boundary planes for all misorientations in the martensitic microstructure. MRD is the multiples of a random distribution.

phenomenological theory of the martensitic phase transformation presented by Bowles and McKenzie [43] was employed to identify the shape deformation relating to each variant and the characteristics of microstructure.

The crystallography of martensite transformation: The Burgers lattice correspondence between the β -phase (bcc crystal structure) and the α -phase (hcp crystal structure) results in the choice of a minimum distortion (the Bain deformation) and rigid body rotation of the parent lattice vectors. To calculate the Bain deformation, the Burgers lattice correspondence is defined based on the orthohexagonal axis systems where a distorted hexagonal crystal can be defined from the parent β -phase (Fig. 9). The Bain strain and the rigid body rotation produce an invariant line strain, which is a result of the implementation of two invariant plane strains (IPS). Therefore, the total transformation strain can be identified by the shape deformation and a shear strain (i.e., lattice invariant deformation).

$$S = BR = PQ \quad (1)$$

Where, S indicates the total transformation strain, B is the Bain strain, R is the rigid body rotation, Q is the lattice-invariant shear and P is the shape deformation associated with the martensitic phase transformation. The complementary shear is to maintain the integrity of the crystal structure (i.e., the deformation must be lattice invariant), which results in reducing the shape change through different shear systems (i.e., twinning and slip). The

Table 1

Individual variants of Burgers OR corresponding to the β matrix and the α product phase [12,19].

Variants	Orientation relationship	Intervariant boundary (from V_1)
1	$(1\bar{1}0)_\beta // (0001)_\alpha$, $[111]_\beta // [11\bar{2}0]$	—
2	$(10\bar{1})_\beta // (0001)_\alpha$, $[111]_\beta // [11\bar{2}0]$	$[11\bar{2}0]/60^\circ$
3	$(01\bar{1})_\beta // (0001)_\alpha$, $[111]_\beta // [11\bar{2}0]$	$[11\bar{2}0]/60^\circ$
4	$(110)_\beta // (0001)_\alpha$, $[\bar{1}11]_\beta // [11\bar{2}0]$	$[1\ 2.38\ 1.38\ 0]/90^\circ$
5	$(101)_\beta // (0001)_\alpha$, $[\bar{1}11]_\beta // [11\bar{2}0]$	$[\bar{1}0\ 5\ 5\ \bar{3}]/63.26^\circ$
6	$(01\bar{1})_\beta // (0001)_\alpha$, $[\bar{1}11]_\beta // [11\bar{2}0]$	$[\bar{1}.377\ \bar{1}\ 2.377\ 0.359]/60.83^\circ$
7	$(110)_\beta // (0001)_\alpha$, $[\bar{1}\bar{1}1]_\beta // [11\bar{2}0]$	$[1\ 2.38\ 1.38\ 0]/90^\circ$
8	$(10\bar{1})_\beta // (0001)_\alpha$, $[\bar{1}\bar{1}1]_\beta // [11\bar{2}0]$	$[\bar{1}.377\ \bar{1}\ 2.377\ 0.359]/60.83^\circ$
9	$(011)_\beta // (0001)_\alpha$, $[\bar{1}\bar{1}1]_\beta // [11\bar{2}0]$	$[\bar{1}0\ 5\ 5\ \bar{3}]/63.26^\circ$
10	$(1\bar{1}0)_\beta // (0001)_\alpha$, $[11\bar{1}]_\beta // [11\bar{2}0]$	$[0\ 0\ 0\ 1]/10.53^\circ$
11	$(101)_\beta // (0001)_\alpha$, $[11\bar{1}]_\beta // [11\bar{2}0]$	$[\bar{1}.377\ \bar{1}\ 2.377\ 0.359]/60.83^\circ$
12	$(011)_\beta // (0001)_\alpha$, $[11\bar{1}]_\beta // [11\bar{2}0]$	$[\bar{1}.377\ \bar{1}\ 2.377\ 0.359]/60.83^\circ$

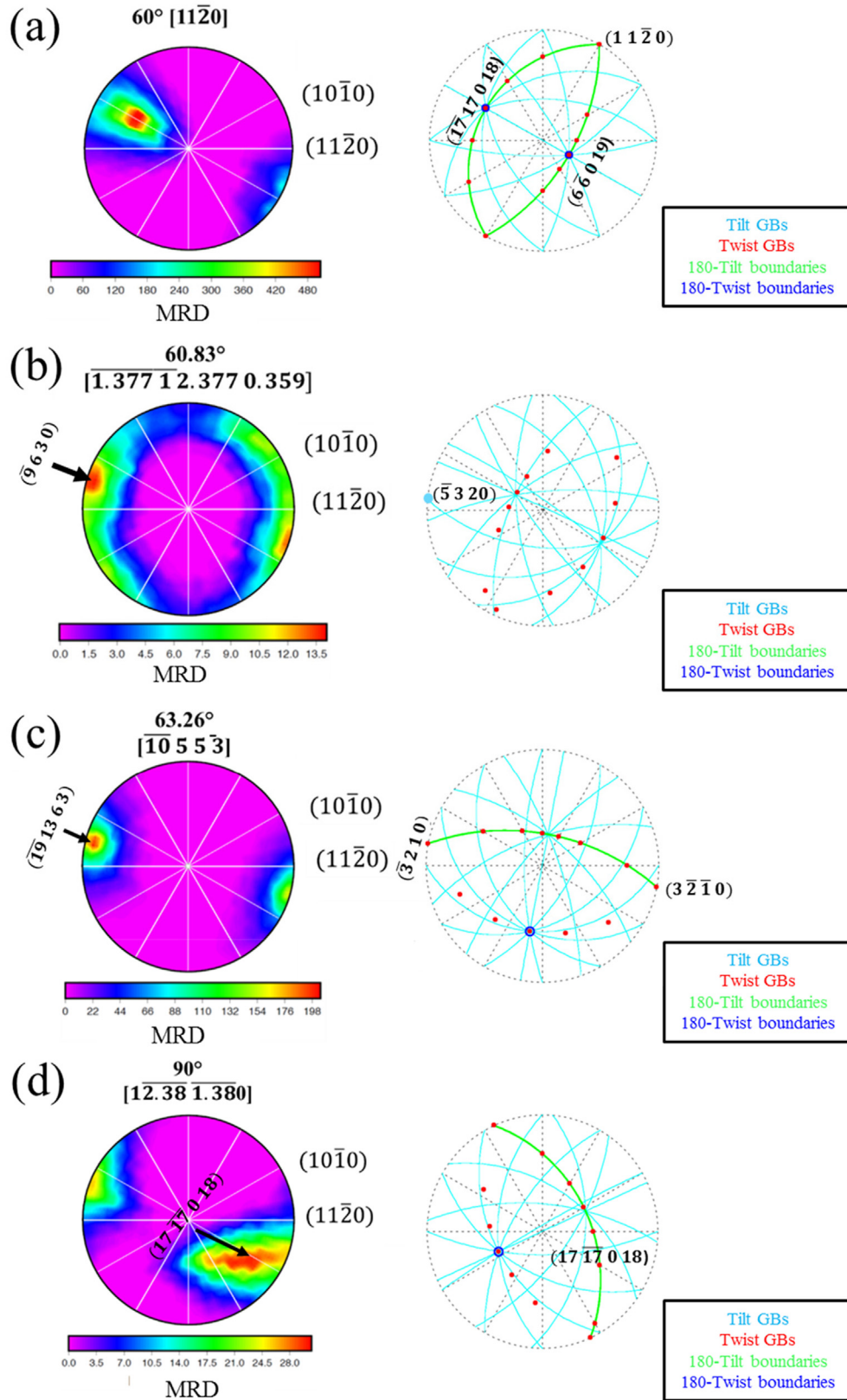


Fig. 7. Distribution of intervariant interface/boundary planes character for different intervariants and the corresponding calculated geometrically characteristic boundaries in the martensitic microstructure.

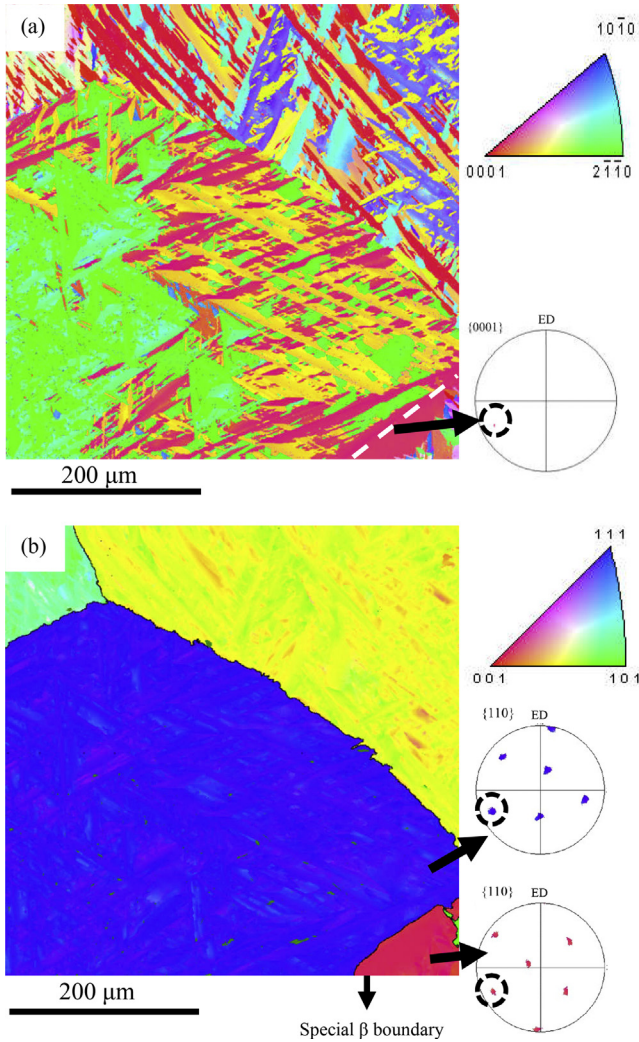


Fig. 8. (a) The IPF map of martensitic microstructure of CP Ti alloy. (b) the corresponding IPF map of reconstructed β -phase of (a), showing the position of prior austenite grain boundaries. The white dash line in (a) represents a special β boundary where two β grains at either side of boundary have a common (110) pole. The triangle insets in (a) and (b) represents the colour codes referred to normal direction. ED represents the extrusion direction. (For interpretation of the references to colour in this figure legend, the reader is referred to the Web version of this article.)

current research assumed possible shear systems given by the Bilby and Crocker inequality [44], provided in Ref. [45], to find out whether the shear system is able to be a lattice invariant strain (LIS). Some of the possible shear systems in the parent and the corresponding product phase, which have been employed in the calculations, are listed in Table 2. These shear systems corresponds to possible slip deformation in titanium alloys [45,46], which make the lattice invariant deformation invisible on the macroscopic scale. A four stage calculation method, presented by Bhadeshia [47], has been employed for calculating the habit plane, and the shape deformation associated with the phase transformation. Each operating shear system mentioned in Table 2 results in four possible habit planes in which the closest habit plane that lies within the experimental $\{334\}$ habit plane [18] was considered for further calculations. Therefore, the shape deformation tensor, the dilatational (δ) and shear components (s) of the transformation can be calculated, as identified in Table 3. Furthermore, the shape deformation tensors (P) of the possible 12 α -variants (mentioned in Table 1) were identified and the corresponding stress tensors (T)

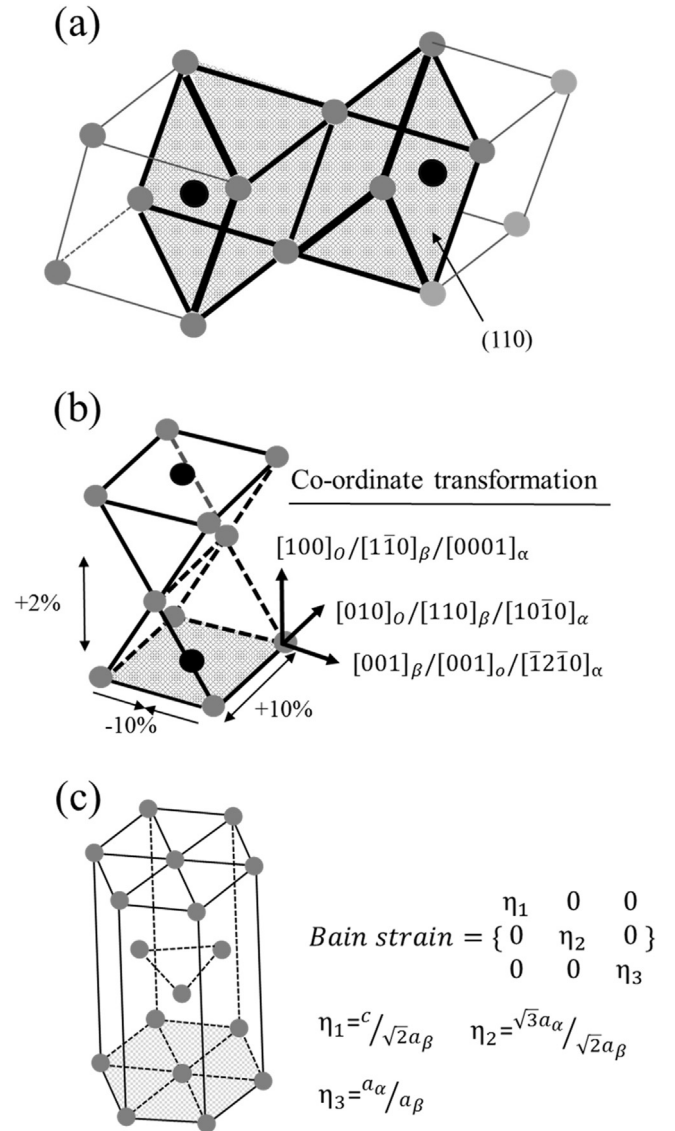


Fig. 9. The orthogonal lattice correspondence between the parent β -phase and daughter α -phase.

were calculated in the following way:

$$T = \frac{P^t P - I}{2} \quad (2)$$

Here, I is a unit matrix and the P^t is the transpose of shape deformation tensor. Finally, the degree of the self-accommodation for different variant combinations can be determined from the Von-Mises equivalent strain (ε_{VM}). The Von-Mises equivalent strain is computed from the overall transformation stress tensors for different variant combinations (i.e., 2-, 3- and 4-variant cluster combinations) in the following way:

$$\varepsilon_{VM} = \sqrt{\frac{2}{3}(T_{11}^2 + T_{22}^2 + T_{33}^2 + \frac{1}{2}(4T_{12}^2 + 4T_{13}^2 + 4T_{23}^2))} \quad (3)$$

The different possible combinations of stress tensors considered in this study are shown in Fig. 10. There are 132, 1320, and 11880 different possible 2-, 3-, and 4-variant combinations, respectively. For each type of variant cluster, the minimum ε_{VM} has been identified and listed in Table 4. The $(1\bar{1}0)_\beta[111]_\beta$ shear system produces

Table 2

The Bilby and Crocker criterion (l and m) for 5 of the possible shear systems in the product hcp martensitic phase for variant 1 [44].

Shear system (S.S) No.	b.c.c		h.c.p		l	m
	Plane	Direction	Plane	Direction		
1	(0 $\bar{1}$ 1)	[$\bar{1}$ 11]	($\bar{1}$ 101)	[$\bar{1}$ 2 $\bar{1}$ 3]	<0	<0
2	($\bar{1}$ 01)	[1 $\bar{1}$ 1]	(10 $\bar{1}$ 1)	[1 $\bar{2}$ 10]	<0	<0
3	(1 $\bar{1}$ 0)	[111]	($\bar{1}$ 101)	[$\bar{1}$ 2 $\bar{1}$ 3]	<0	<0
4	(0 $\bar{1}$ 1)	[111]	(10 $\bar{1}$ 1)	[2 $\bar{1}$ 13]	<0	<0
5	(10 $\bar{1}$)	[111]	(10 $\bar{1}$ 1)	[2 $\bar{1}$ 13]	<0	<0

the lowest Von-Mises equivalent strain for all types of variant cluster combinations. Interestingly, the three variant cluster has the minimum ϵ_{VM} (0.0011) resulting in 4 possible 3-variant clusters (i.e., $V_1V_2V_3$, $V_4V_5V_6$, $V_7V_8V_9$ and $V_{10}V_{11}V_{12}$). The nearest equivalent strain for the other shear systems mentioned in this study provided values of at least an order of magnitude higher than the calculated values for the $(1\bar{1}0)_\beta[111]_\beta$ shear system. This means that the reduction of strain energy during the martensite transformation leads to a lattice invariant deformation, by the $(1\bar{1}0)_\beta[111]_\beta$ slip system. Therefore, to minimise strain energy, the transformation preferentially produces 3-variant cluster with a triangular morphology, as seen in Fig. 3. In different alloys that also undergo a bcc to hcp martensitic phase transformation, this is known as a self-accommodation morphology [12,18,48].

According to Fig. 3, the triangular morphology is initially formed by the large martensitic laths and the space needed for the newly nucleated variants decreases as the transformation proceeds. This ultimately leads to a smaller cluster size. In some parts of the microstructure, 2-variant clusters are also observed as twin related parallel laths (Fig. 3c). However, according to Table 4, the lowest equivalent strain (ϵ_{VM}) for a 2-variant cluster is an order of magnitude higher than the three-variant cluster. Therefore, the twinned lath morphology might be a sectioning artefact and appear when a pyramid shaped stack of 3-variant clusters is sectioned in such a way that only two of the variants lie in the section plane.

Contrary to the current observations, Wang et al. [12] reported two types of 3- and 4-variant clusters for the martensitic transformation in pure Ti. This discrepancy most likely arises from the way the transformation strain accommodation is calculated. In the previous work, only the shear component of the strain reduction was used to predict the possible variant combinations. In the current study, the reduction of both the dilatation and shear components of the shape strain (the Von-Mises criteria) are used to

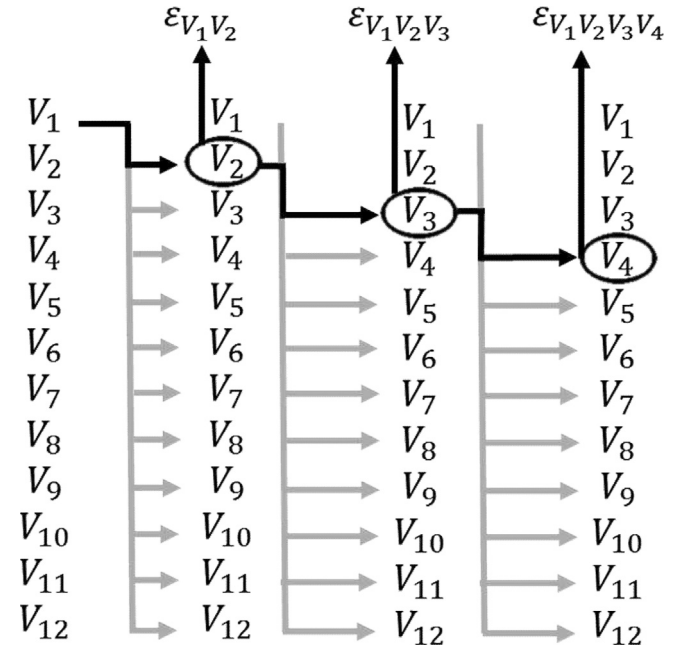


Fig. 10. The calculation of ϵ_{VM} for different 2, 3 and 4 variant cluster combinations using Von Mises criteria.

determine the probable variant cluster combinations. The latter appears to be more consistent with the current martensitic microstructure, where it mostly consists of 3-variant clusters. This suggests that it is essential to consider the relaxation of all shape strain components to better predict the variant selection mechanism in the martensitic transformation.

Theoretically, the combination of three consecutive variants results in the formation of $60^\circ/[11\bar{2}0]$ intervariant boundaries (Table 1). Accordingly, the variants in the observed clusters are separated by the $60^\circ/[11\bar{2}0]$ boundaries (Fig. 11) leading to a significant population (60%) in the martensitic microstructure (Fig. 5b). Interestingly, the most populated intervariant boundary in a case of a Ti-6Al-4V alloy [19] was reported to be $63.85^\circ/[1\bar{0}55\bar{3}]$. This may suggest that the chemical composition can alter the Bain deformation (by changing the lattice parameters) during the martensite transformation and consequently vary the variant cluster arrangement/s. Moreover, as Fig. 11 suggests, the intersection of two clusters results in the formation of other

Table 3

The typical calculated crystallographic sets considering the activation of different shear system numbers (S.S No.).

S.S No.	Habit plane (p)	Invariant line strain (S)	Shape deformation (P2)	δ and s
1	$\begin{pmatrix} 0.497 \\ 0.519 \\ 0.696 \end{pmatrix}$	$\begin{pmatrix} 1.044 & 0.0371 & 0.0955 \\ 0.0452 & 1.0495 & 0.0509 \\ 0.0798 & 0.0808 & 0.8746 \end{pmatrix}$	$\begin{pmatrix} 1.062 & 0.064 & 0.086 \\ 0.038 & 1.039 & 0.053 \\ 0.088 & 0.092 & 0.877 \end{pmatrix}$	$\delta = 0.022$ $s = 0.228$
2	$\begin{pmatrix} 0.489 \\ 0.4948 \\ 0.7163 \end{pmatrix}$	$\begin{pmatrix} 1.0451 & 0.0431 & 0.0637 \\ 0.0426 & 1.0452 & 0.0625 \\ 0.0781 & 0.0766 & 0.8879 \end{pmatrix}$	$\begin{pmatrix} 1.0418 & 0.0423 & 0.0611 \\ 0.0441 & 1.0446 & 0.0647 \\ 0.0749 & 0.0758 & 0.8903 \end{pmatrix}$	$\delta = 0.023$ $s = 0.1935$
3	$\begin{pmatrix} 0.4258 \\ 0.5604 \\ 0.7115 \end{pmatrix}$	$\begin{pmatrix} 1.0454 & 0.0179 & 0.450 \\ 0.0680 & 1.0449 & 0.0809 \\ 0.0594 & 0.0965 & 0.8877 \end{pmatrix}$	$\begin{pmatrix} 1.02722 & 0.0036 & 0.0455 \\ 0.0486 & 1.0639 & 0.0811 \\ 0.0673 & 0.0885 & 0.8876 \end{pmatrix}$	$\delta = 0.021$ $s = 0.169$
4	$\begin{pmatrix} 0.4903 \\ 0.383 \\ 0.779 \end{pmatrix}$	$\begin{pmatrix} 1.0470 & 0.0625 & 0.0478 \\ 0.0275 & 1.0467 & 0.0187 \\ 0.0567 & 0.0255 & 0.8915 \end{pmatrix}$	$\begin{pmatrix} 0.9533 & -0.036 & -0.074 \\ 0.027 & 1.1021 & 0.044 \\ -0.056 & -0.044 & 0.911 \end{pmatrix}$	$\delta = 0.0216$ $s = 0.1384$
5	$\begin{pmatrix} 0.4707 \\ 0.4991 \\ 0.7280 \end{pmatrix}$	$\begin{pmatrix} 1.0369 & 0.0255 & 0.0262 \\ 0.0555 & 1.0468 & 0.0523 \\ 0.0468 & 0.0598 & 0.9054 \end{pmatrix}$	$\begin{pmatrix} 0.945 & 0.0584 & 0.0851 \\ 0.0963 & 1.10207 & 0.1488 \\ 0.1253 & 0.1328 & 1.1937 \end{pmatrix}$	$\delta = 0.1467$ $s = 0.3237$

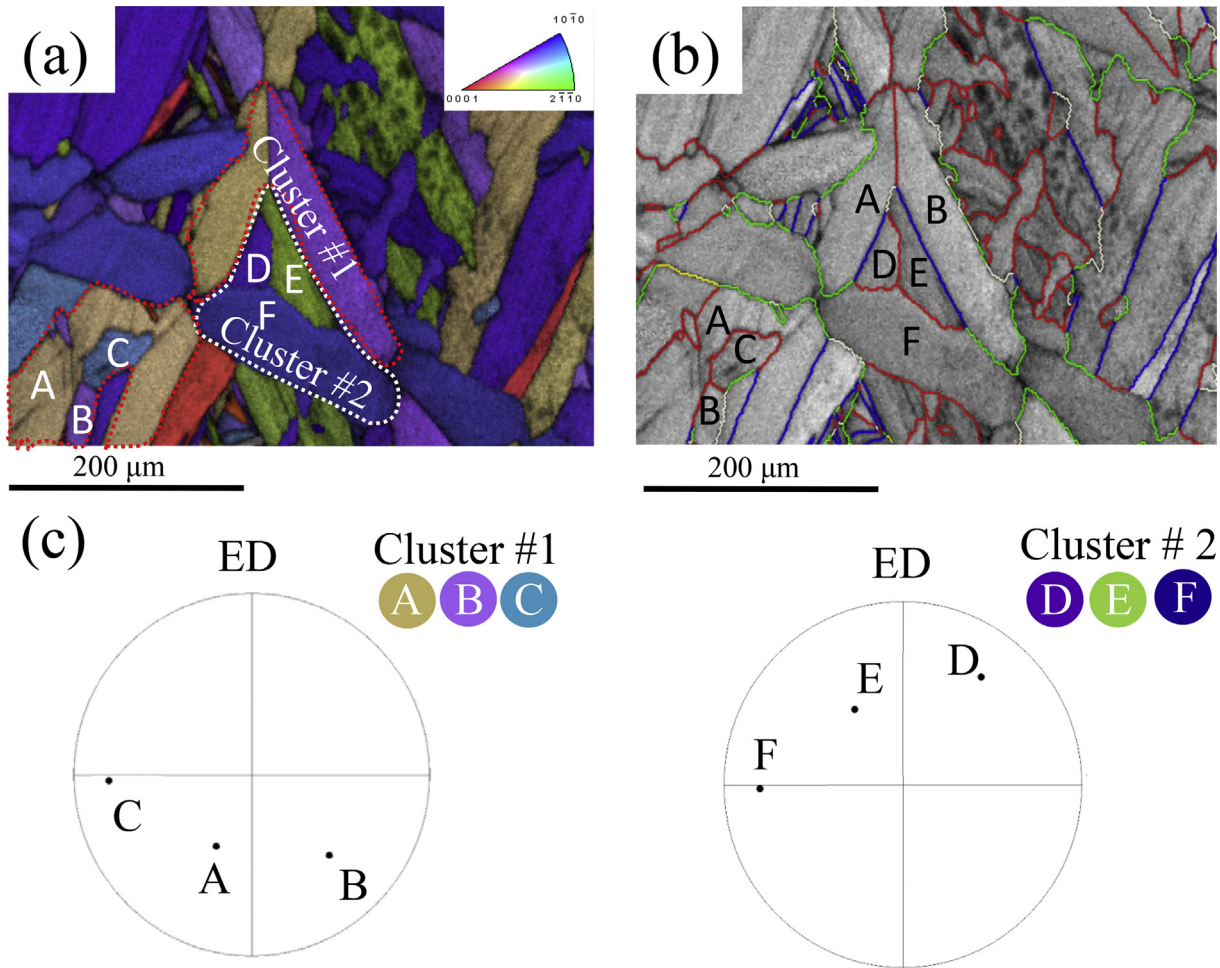


Fig. 11. The IPF (a) and corresponding band contrast (b) images showing three variant clustering in the martensitic microstructure. Yellow, red, green, blue and white lines in (b) are the $10.53^\circ/[0001]$, $60^\circ/[11\bar{2}0]$, $60.83^\circ/[\bar{1}377\bar{1}2.377\ 0.359]$, $63.26^\circ/[\bar{1}0\ 5\ 5\ \bar{3}]$ and $90^\circ/[1\bar{2}38\ 1.380]$ intervariant boundaries, respectively. A, B, C and D,E,F labels in (a) and (b) represent 3-variant clusters of 1 and 2, respectively, as plotted in (0001) pole figures (c). The triangle inset in (a) represents the colour codes referred to normal direction. (For interpretation of the references to colour in this figure legend, the reader is referred to the Web version of this article.)

interplanar spacing (i.e., 1.8019 Å, Table 5), suggesting a relatively low energy configuration. This is consistent with the molecular dynamics energy calculation [5], showing that the pyramidal ($\bar{1}101$) plane has the minimum energy (168.7 mJ/m²) among the $[11\bar{2}0]$ tilt boundaries. Interestingly, the other sets of planes predicted to have low energies by the calculation, such as ($\bar{1}013$,

$\bar{1}012$) and ($\bar{2}021$) at rotation angles of 31.39° , 42.47° and 74.7° , respectively, are absent from the misorientation angle distribution of the martensite sample. This suggests that the martensitic transformation in commercially pure Ti and the associated crystallographic constraints can simultaneously provide low energy configurations in the form of three-variant clusters terminating on

Table 5

The interplanar spacing (d_{hkl}) for different measured intervariant planes and their corresponding population.

Intervariant boundary		Intensity (MRD)	Interplanar spacing (Å)	
Axis/Angle	Plane			
Fig. 6	All boundaries	$(1\ 0\ \bar{1}\ 0)$	1.5	0.8519 or 1.7038 ^a
		$(1\ 1\ \bar{2}\ 0)$	1	1.4755
		$(0\ 0\ 0\ 1)$	0.36	2.0283
		$(1\ 0\ \bar{1}\ 1)$	1.62	0.3604 or 1.8019 ^a
		$(4\ \bar{1}\ \bar{3}\ 0)$	1.62	0.2363 or 0.4725 ^a
Fig. 7	$10.53^\circ/[0\ 0\ 0\ 1]$	$(19\ \bar{8}\ \bar{1}\ \bar{1}\ 0)$	0.49	0.1547
		$(\bar{1}\ 1\ 0\ 1)$	504.0	0.3604 or 1.8019 ^a
		$(\bar{9}\ 6\ 3\ 0)$	14.01	0.3219
		$(\bar{5}\ 3\ 2\ 0)$	12.00	0.1954 or 0.3908 ^a
		$(\bar{3}\ 2\ 1\ 0)$	160.73	0.3219 or 0.6439 ^a
		$(\bar{19}\ 13\ 6\ 3)$	204.21	0.0251 or 0.1258 ^a
		$(17\ \bar{1}\ \bar{7}\ 0\ 18)$	30.68	0.0416 or 0.0833 ^a
$60^\circ/[1\ 1\ \bar{2}\ 0]$				
$60.83^\circ/[\bar{1}377\bar{1}2.377\ 0.359]$				
$63.26^\circ/[\bar{1}0\ 5\ 5\ \bar{3}]$				
$90^\circ/[1\ \bar{2}38\ 1.38\ 0]$				

^a Taking into account the structure factor as the plane passing through an additional atom [57].

pyramidal planes. In other words, the $60^\circ/[11\bar{2}0]$ with low energy $(\bar{1}101)$ plane accounts for ~60% of total boundary area in the microstructure. The other intervariant boundaries reveal higher energy configurations resulting from the intersection of these triangular clusters (e.g., $63.26^\circ/[10\bar{5}5\bar{3}]$ intervariant boundaries terminated on $\{\bar{1}9\ 13\ 6\ 3\}$ planes, Fig. 7c).

5. Conclusion

In the current study, the characteristics of intervariant boundaries in commercially pure Ti subjected to the martensitic transformation were investigated by conventional EBSD mapping and a five parameter analysis of the boundary data. The following summarises the most important findings drawn from this investigation:

- The as-received and transformed microstructures had similar textures, with the (0001) pole figure revealing multiple peaks perpendicular to the extrusion direction. However, because of variant multiplication, the martensitic transformation decreased the strength of the texture.
- The grain boundary misorientation angle distribution revealed four distinct peaks closely associated with the theoretical intervariant boundaries expected from the Burgers orientation relationship. The $60^\circ/[11\bar{2}0]$ intervariant boundary made up 60% of the boundary area.
- Three-variant clusters separated by $60^\circ/[11\bar{2}0]$ boundaries frequently appeared in the martensitic microstructure. According to the phenomenological theory of martensite, this specific triangular morphology minimises the transformation strain compared to other possible cluster arrangements involving four or fewer variants.
- The grain boundary plane distribution, ignoring misorientation, is strongly anisotropic with most boundaries terminated on the prismatic $\{hki0\}$ and pyramidal $(\bar{1}101)$ planes. The $(\bar{1}101)$ boundary orientations are associated with the symmetric tilt $60^\circ/[11\bar{2}0]$ intervariant boundaries. The other intervariant boundaries expected from the Burgers orientation relationship largely terminated on prismatic planes, but did not necessarily have low energy interface arrangements.

Acknowledgements

Deakin University's Advanced Characterization Facility is acknowledged for use of the EBSD instruments and assistance from Dr. Mark Nave. The authors thank Dr. Lionel Germain of the Lorraine University for his assistance on back-calculation of EBSD data.

Appendix

A.1 Phenomenological theory of martensite transformation

Based on the phenomenological theory of martensite introduced by Mackenzie and Bowles [60], it has been shown that the total atomic displacements and the transformation strain has the characteristic of an invariant plain strain, which leaves the habit plane invariant (i.e., undistorted and unrotated). The magnitude m of the shape deformation can be determined as its unit displacement vector d . The habit plane of the martensite (unit normal p) is the invariant–plane of the shape deformation. The shape deformation can be represented by means of a shape deformation matrix P :

$$P = I + m[d](p) \quad (4)$$

Where the basis is chosen to be orthonormal, although the

equation is valid for any basis.

However, the invariant plane strain, IPS, cannot solely change the structure of a bcc structure into a hcp structure. On the contrary, an invariant line strain (ILS) can accommodate the phase structure change associated with the martensite transformation. The ILS can be factorised into two plain strains. Therefore, another invariant plane Q , which is considered as a complementary simple shear, with the magnitude of n on a plane with unit normal of q and in a unit direction of e accompanies the shape deformation:

$$Q = I + n[e](q) \quad (5)$$

Therefore, the invariant line strain is identified by two homogeneous invariant plane strains in a way that $S = P.Q$. However, the shape change due to the simple shear Q is rendered invisible on a macroscopic scale since there is also an inhomogeneous lattice-invariant deformation, which can be slip or twinning. This cancels out the shape change due to Q , without altering the lattice structure. The macroscopic shape change is solely due to P and therefore has the characteristics of an invariant–plane strain, as experimentally observed. The transformation strain, S , can be factorised into a Bain strain, B , combined with an appropriate rigid body rotation, R , such that $S = R.B$. The invariant–line of transformation strain lies in the planes p and q , and the invariant–normal of S defines a plane containing d and e . Hence:

$$S = R.B = P.Q \quad (6)$$

A.2. Determination of lattice transformation strain

The deformation matrix representing the Bain strain, which carries the bcc β -lattice to the hcp α -lattice in an orthonormal basis (Fig. 9) is given by:

$$B = \left\{ \begin{array}{ccc} \eta_1 = c_h/\sqrt{2}a_b & 0 & 0 \\ 0 & \eta_2 = \sqrt{3}a_h/\sqrt{2}a_b & 0 \\ 0 & 0 & \eta_3 = a_h/a_b \end{array} \right\} \quad (7)$$

To find the rigid body rotation, first the invariant line and invariant plane normal should be identified, based on the condition that the invariant line of S must lie within the shear plane to cancel the complementary shear Q . Therefore, the unit vector of $[u] = [u_1 u_2 u_3]$ must lie in the shear plane (w) = ($w_1 w_2 w_3$) meaning:

$$w_1 u_1 + w_2 u_2 + w_3 u_3 = 0 \quad (8)$$

The magnitude of the $[F; u]$ prior to the deformation is:

$$|u^2| = u_1^2 + u_2^2 + u_3^2 = 1 \quad (9)$$

The Bain strain takes $[u] = [u_1 u_2 u_3]$ in the orthonormal reference frame into $[x] = [x_1 x_2 x_3]$. As a result the deformation u becomes a new vector x but the magnitude of the vector remains unchanged (i.e., $[u] = B.[x]$). Therefore;

$$u_1^2 + u_2^2 + u_3^2 = \eta_1^2 u_1^2 + \eta_2^2 u_2^2 + \eta_3^2 u_3^2 \quad (10)$$

Equations (8)–(10) can be solved and give two solutions for the undistorted line. Consequently, for the invariant normal of the invariant lattice strain, the invariant plane (h) = ($h_1 h_2 h_3$) should contain the shear direction $[r] = [r_1 r_2 r_3]$. Then;

$$r_1 h_1 + r_2 h_2 + r_3 h_3 = 0 \quad (11)$$

Furthermore;

$$|h^2| = h_1^2 + h_2^2 + h_3^2 = 1 \quad (12)$$

The lattice deformation (i.e., Bain deformation) converts (h) to (l) = (h) B^{-1} . Therefore;

$$h_1^2 + h_2^2 + h_3^2 = h_1^2/\eta_1^2 + h_2^2/\eta_2^2 + h_3^2/\eta_3^2 \quad (13)$$

Consequently, equations (11)–(13) can be solved to give two solutions for the undistorted normal. To convert the Bain strain into an invariant line strain, S , the rigid body rotation, R , must be employed, bringing an undistorted line (i.e., $[x]$) and undistorted normal (i.e., (h)) back into the original direction along with the $[u]$ and (h). For both $[x]$ and (l), there are two solutions. Therefore, there would be four solutions for converting B into S .

$$x = Bu \quad l = hB^{-1} \quad (14)$$

Also, the cross product of (h) and $[u]$ (i.e., $u \times h = a$) is converted (i.e., $x \times l = b$) into S after the Bain deformation [47]. Therefore, the rigid body rotation can be obtained through the following equations:

$$u = R.x \quad h = R.l \quad a = R.b \quad (15)$$

By converting these equations into a 3×3 matrix, they can be defined as:

$$\begin{pmatrix} u_1 & h_1 & a_1 \\ u_2 & h_2 & a_2 \\ u_3 & h_3 & a_3 \end{pmatrix} = \begin{pmatrix} R_{11} & R_{12} & R_{13} \\ R_{21} & R_{22} & R_{23} \\ R_{31} & R_{32} & R_{33} \end{pmatrix} \begin{pmatrix} x_1 & l_1 & b_1 \\ x_2 & l_2 & b_2 \\ x_3 & l_3 & b_3 \end{pmatrix} \quad (16)$$

Here, R , B and S are explained in the orthogonal coordinate system (Fig. 9) and they can be defined in parent (i.e., β) coordinate, as below:

$$B_\beta = T^{-1}B_0T \quad R_\beta = T^{-1}R_0T \quad S_\beta = R_\beta B_\beta \quad (17)$$

The transformation matrix can be described as:

$$T = \begin{bmatrix} 1/\sqrt{2} & -1/\sqrt{2} & 0 \\ 1/\sqrt{2} & 1/\sqrt{2} & 0 \\ 0 & 0 & 1 \end{bmatrix} \quad (18)$$

A.3. Calculating the habit plane and the shape deformation

The habit plane (i.e., unit normal, p) can be solved through equations (4)–(6), considering the fact that S is an invariant line strain. In addition, the invariant line $[u]$ of S must lie in shear plane (w) and the invariant-normal (h), containing the shear direction $[r]$. Therefore, the habit plane must be compatible with the chosen lattice shear system. Considering equations (4)–(6), the habit plane can be given by normalization of equation (19):

$$(p) = (w) - (q)S^{-1} \quad (19)$$

Now to completely define the shape deformation, the values of $[d]$ and m in equation (6) should be identified, as below:

$$cm[d] = S[e] - [e] \quad (20)$$

Here, c is dot product of the habit plane and $[e]$, and m is the

magnitude of the involved displacement, which is factorised into a shear component s ($s = (m^2 - \delta^2)$) parallel to the habit plane and a dilatational component δ ($\delta = m[d] \cdot (p)$). Note that e is the shear on the direction where the Q (complementary shear) is being canceled out ($[e] = [\bar{r}]$).

Hence, the homogenous shear (Q) can be identified, as below:

$$Q = P^{-1}.S \quad (21)$$

References

- [1] Y. Guo, T.B. Britton, A.J. Wilkinson, Slip band-grain boundary interactions in commercial-purity titanium, *Acta Mater.* 76 (2014) 1–12, <https://doi.org/10.1016/j.actamat.2014.05.015>.
- [2] D.T. Powell, J.C. Scully, Stress corrosion cracking of alpha titanium alloys at room temperature, *Corrosion* 24 (1968) 151–158.
- [3] D.S. Shih, I.M. Robertson, H.K. Birnbaum, Hydrogen embrittlement of α titanium: in situ tem studies, *Acta Metall.* 36 (1988) 111–124, [https://doi.org/10.1016/0001-6160\(88\)90032-6](https://doi.org/10.1016/0001-6160(88)90032-6).
- [4] H. Ghonem, Microstructure and fatigue crack growth mechanisms in high temperature titanium alloys, *Int. J. Fatig.* 32 (2010) 1448–1460, <https://doi.org/10.1016/j.ijfatigue.2010.02.001>.
- [5] J. Wang, I.J. Beyerlein, Atomic structures of symmetric tilt grain boundaries in hexagonal close packed (hcp) crystals, *Model. Simulat. Mater. Sci. Eng.* 20 (2012) 24002.
- [6] L. Capolungo, I.J. Beyerlein, G.C. Kaschner, C.N. Tomé, On the interaction between slip dislocations and twins in HCP Zr, *Mater. Sci. Eng.* 513–514 (2009) 4465–4481, <https://doi.org/10.1016/j.msea.2009.01.035>.
- [7] A. Serra, D.J. Bacon, Computer simulation of screw dislocation interactions with twin boundaries in H.C.P. metals, *Acta Metall. Mater.* 43 (1995) 4465–4481, [https://doi.org/10.1016/0956-7151\(95\)00128-1](https://doi.org/10.1016/0956-7151(95)00128-1).
- [8] A. Serra, D.J. Bacon, R.C. Pond, Twins as barriers to basal slip in hexagonal-close-packed metals, *Met. Mater. Trans. A* 33 (2002) 809–812, <https://doi.org/10.1007/s11661-002-1012-6>.
- [9] J. Wang, L. Liu, C.N. Tomé, S.X. Mao, S.K. Gong, Twinning and de-twinning via glide and climb of twinning dislocations along serrated coherent twin boundaries in hexagonal-close-packed metals, *Mater. Res. Lett.* 1 (2013) 81–88, <https://doi.org/10.1080/21663831.2013.779601>.
- [10] W.G. Burgers, On the process of transition of the cubic-body-centered modification into the hexagonal-close-packed modification of zirconium, *Physica* 1 (1934) 561–586, [https://doi.org/10.1016/S0031-8914\(34\)80244-3](https://doi.org/10.1016/S0031-8914(34)80244-3).
- [11] A.G. Khundzhua, A.G. Ptitsyn, E.A. Brovkina, S. Chzhen, Self-accommodation of crystals of martensitic phases in titanium and zirconium based alloys, *Phys. Met. Metallogr.* 113 (2012) 1035–1040, <https://doi.org/10.1134/s0031918x12110117>.
- [12] S.C. Wang, M. Aindow, M.J. Starink, Effect of self-accommodation on α/α boundary populations in pure titanium, *Acta Mater.* 51 (2003) 2485–2503, [https://doi.org/10.1016/S1359-6454\(03\)00035-1](https://doi.org/10.1016/S1359-6454(03)00035-1).
- [13] M. Shibata, K. Ono, On the minimization of strain energy in the martensitic transformation of titanium, *Acta Metall.* 25 (1977) 35–42, [https://doi.org/10.1016/0001-6160\(77\)90243-7](https://doi.org/10.1016/0001-6160(77)90243-7).
- [14] T. Furuhashi, T. Maki, Variant selection in heterogeneous nucleation on defects in diffusional phase transformation and precipitation, *Mater. Sci. Eng., A* 312 (2001) 145–154, [https://doi.org/10.1016/S0921-5093\(00\)01904-3](https://doi.org/10.1016/S0921-5093(00)01904-3).
- [15] H. Moustahfid, N. Gey, Study of the β - α phase transformations of a Ti-64 sheet induced from a high-temperature β state and a high-temperature α + β state, *Metall. Mater. Trans. A* 28 (1997) 51–61, <https://doi.org/10.1007/s11661-997-0082-x>.
- [16] N. Gey, M. Humbert, Characterization of the variant selection occurring during the α to β phase transformations of a cold rolled titanium sheet, *Acta Mater.* 50 (2002) 277–287, [https://doi.org/10.1016/S1359-6454\(01\)00351-2](https://doi.org/10.1016/S1359-6454(01)00351-2).
- [17] D. Qiu, R. Shi, D. Zhang, W. Lu, Y. Wang, Variant selection by dislocations during α precipitation in α/β titanium alloys, *Acta Mater.* 88 (2015) 218–231, <https://doi.org/10.1016/j.actamat.2014.12.044>.
- [18] D. Srivastava, K. Madangopal, S. Banerjee, S. Ranganathan, Self accommodation morphology of martensite variants in Zr-2.5wt % Nb alloy, *Acta Metall. Mater.* 41 (1993) 3445–3454.
- [19] H. Beladi, Q. Chao, G.S. Rohrer, Variant selection and intervariant crystallographic planes distribution in martensite in a Ti-6Al-4V alloy, *Acta Mater.* 80 (2014) 478–489, <https://doi.org/10.1016/j.actamat.2014.06.064>.
- [20] G.S. Rohrer, D.M. Saylor, B. El Dasher, B.L. Adams, A.D. Rollet, P. Wynblatt, The distribution of internal interfaces in polycrystals, *Zeitschrift Für Met* 95 (2004) 197–214, <https://doi.org/10.3139/146.017934>.
- [21] G. Lütjering, J.C. Williams, *Titanium*, Springer Science & Business Media, 2007.
- [22] G. Welsch, R. Boyer, E.W. Collings, *Materials Properties Handbook: Titanium Alloys*, ASM international, 1993.
- [23] D.M. Saylor, B.S. El-Dasher, B.L. Adams, G.S. Rohrer, Measuring the five-parameter grain-boundary distribution from observations of planar sections, *Metall. Mater. Trans. A* 35 (2004) 1981–1989, <https://doi.org/10.1007>

- s11661-004-0147-z.
- [24] H. Beladi, G.S. Rohrer, A.D. Rollett, V. Tari, P.D. Hodgson, The distribution of intervariant crystallographic planes in a lath martensite using five macroscopic parameters, *Acta Mater.* 63 (2014) 86–98, <https://doi.org/10.1016/j.actamat.2013.10.010>.
- [25] H. Beladi, G.S. Rohrer, The relative grain boundary area and energy distributions in a ferritic steel determined from three-dimensional electron backscatter diffraction maps, *Acta Mater.* 61 (2013) 1404–1412, <https://doi.org/10.1016/j.actamat.2012.11.017>.
- [26] H. Beladi, N.T. Nuhfer, G.S. Rohrer, The five-parameter grain boundary character and energy distributions of a fully austenitic high-manganese steel using three dimensional data, *Acta Mater.* 70 (2014) 281–289, <https://doi.org/10.1016/j.actamat.2014.02.038>.
- [27] H. Beladi, G.S. Rohrer, The distribution of grain boundary planes in interstitial free steel, *Metall. Mater. Trans. A Phys. Metall. Mater. Sci.* 44 (2013) 115–124, <https://doi.org/10.1007/s11661-012-1393-0>.
- [28] H. Beladi, G.S. Rohrer, The role of thermomechanical routes on the distribution of grain boundary and interface plane orientations in transformed microstructures, *Metall. Mater. Trans. A* 48 (2017) 2781–2790, <https://doi.org/10.1007/s11661-016-3630-4>.
- [29] S. Ratanaphan, Y. Yoon, G.S. Rohrer, The five parameter grain boundary character distribution of polycrystalline silicon, *J. Mater. Sci.* 49 (2014) 4938–4945, <https://doi.org/10.1007/s10853-014-8195-2>.
- [30] M.R. Daymond, R.A. Holt, S. Cai, P. Mosbrucker, S.C. Vogel, Texture inheritance and variant selection through an hcp-bcc-hcp phase transformation, *Acta Mater.* 58 (2010) 4053–4066, <https://doi.org/10.1016/j.actamat.2010.03.012>.
- [31] K. Glowinski, A. Morawiec, A toolbox for geometric grain boundary characterization, in: *Proc. 1st Int. Conf. 3D Mater. Sci.*, Springer, Cham, 2012, pp. 119–124.
- [32] T. Tomida, M. Wakita, M. Yasuyama, S. Sugaya, Y. Tomota, S.C. Vogel, Memory effects of transformation textures in steel and its prediction by the double Kurdjumov-Sachs relation, *Acta Mater.* 61 (2013) 2828–2839, <https://doi.org/10.1016/j.actamat.2013.01.015>.
- [33] N. Stanford, P.S. Bate, Crystallographic variant selection in Ti-6Al-4V, *Acta Mater.* 52 (2004) 5215–5224, <https://doi.org/10.1016/j.actamat.2004.07.034>.
- [34] G.C. Obasi, S. Biroscas, J. Quinta Da Fonseca, M. Preuss, Effect of β grain growth on variant selection and texture memory effect during $\alpha \rightarrow \beta \rightarrow \alpha$ phase transformation in Ti-6 Al-4 v, *Acta Mater.* 60 (2012) 1048–1058, <https://doi.org/10.1016/j.actamat.2011.10.038>.
- [35] G.C. Obasi, J.Q. da Fonseca, D. Rugg, M. Preuss, The effect of β grain coarsening on variant selection and texture evolution in a near- β Ti alloy, *Mater. Sci. Eng., A* 576 (2013) 272–279, <https://doi.org/10.1016/j.msea.2013.04.018>.
- [36] D. Bhattacharyya, G.B. Viswanathan, H.L. Fraser, Crystallographic and morphological relationships between β phase and the Widmanstatten and allotriomorphic α phase at special β grain boundaries in an α/β titanium alloy, *Acta Mater.* 55 (2007) 6765–6778, <https://doi.org/10.1016/j.actamat.2007.08.029>.
- [37] E. Lee, R. Banerjee, S. Kar, D. Bhattacharyya, H.L. Fraser, Selection of α variants during microstructural evolution in α/β titanium alloys, *Philos. Mag* 87 (2007) 3615–3627, <https://doi.org/10.1080/14786430701373672>.
- [38] L. Germain, S.R. Dey, M. Humbert, N. Gey, Determination of parent orientation maps in advanced titanium-based alloys, *J. Microsc.* 227 (2007) 284–291, <https://doi.org/10.1111/j.1365-2818.2007.01812.x>.
- [39] R. Shi, V. Dixit, H.L. Fraser, Y. Wang, Variant selection of grain boundary α by special prior β grain boundaries in titanium alloys, *Acta Mater.* 75 (2014) 156–166, <https://doi.org/10.1016/j.actamat.2014.05.003>.
- [40] J. Romero, M. Preuss, J. Quinta da Fonseca, Texture memory and variant selection during phase transformation of a zirconium alloy, *Acta Mater.* 57 (2009) 5501–5511, <https://doi.org/10.1016/j.actamat.2009.07.046>.
- [41] S. Banerjee, P. Mukhopadhyay, *Phase Transformations: Examples from Titanium and Zirconium Alloys*, Elsevier, 2010.
- [42] K. Otsuka, C.M. Wayman, *Shape Memory Materials*, Cambridge university press, 1999.
- [43] J.S. Bowles, J.K. Mackenzie, The crystallography of martensite transformations I, *Acta Mater.* 2 (1954) 129–137, [https://doi.org/10.1016/0001-6160\(54\)90102-9](https://doi.org/10.1016/0001-6160(54)90102-9).
- [44] A.G. Crocker, B.A. Bilby, *The crystallography of the martensite reaction in steel*, *Acta Metall.* 9 (1961) 678–688.
- [45] S. Banerjee, P. Mukhopadhyay, Martensitic transformations, in: *Phase Transform. Examples from Titan. Zircon. Alloy.*, first ed., Elsevier, 2007, pp. 259–376, <https://doi.org/10.1002/0471749311.ch24>.
- [46] G. Lütjering, J.C. Williams, *Titanium*, second ed., Springer-Verlag Berlin Heidelberg, 2007 <https://doi.org/10.1007/978-3-540-73036-1>.
- [47] H. Bhadeshia, *Geometry of Crystals*, Inst. Mater, London, 2001.
- [48] Y.W. Chai, H.Y. Kim, H. Hosoda, S. Miyazaki, Self-accommodation in Ti-Nb shape memory alloys, *Acta Mater.* 57 (2009) 4054–4064, <https://doi.org/10.1016/j.actamat.2009.04.051>.
- [49] J. Gruber, D.C. George, A.P. Kuprat, G.S. Rohrer, A.D. Rollett, Effect of anisotropic grain boundary properties on grain boundary plane distributions during grain growth, *Scripta Mater.* 53 (2005) 351–355, <https://doi.org/10.1016/j.scriptamat.2005.04.004>.
- [50] J. Gruber, H.M. Miller, T.D. Hoffmann, G.S. Rohrer, A.D. Rollett, Misorientation texture development during grain growth. Part I: simulation and experiment, *Acta Mater.* 57 (2009) 6102–6112, <https://doi.org/10.1016/j.actamat.2009.08.036>.
- [51] S. Ratanaphan, D.L. Olmsted, V.V. Bulatov, E.A. Holm, A.D. Rollett, G.S. Rohrer, Grain boundary energies in body-centered cubic metals, *Acta Mater.* 88 (2015) 346–354, <https://doi.org/10.1016/j.actamat.2015.01.069>.
- [52] S.J. Dillon, G.S. Rohrer, Mechanism for the development of anisotropic grain boundary character distributions during normal grain growth, *Acta Mater.* 57 (2009) 1–7, <https://doi.org/10.1016/j.actamat.2008.08.062>.
- [53] J. Li, S.J. Dillon, G.S. Rohrer, Relative grain boundary area and energy distributions in nickel, *Acta Mater.* 57 (2009) 4304–4311, <https://doi.org/10.1016/j.actamat.2009.06.004>.
- [54] G.S. Rohrer, J. Li, S. Lee, A.D. Rollett, M. Groeber, M.D. Uchic, Deriving grain boundary character distributions and relative grain boundary energies from three-dimensional EBSD data, *Mater. Sci. Technol.* 26 (2010) 661–669, <https://doi.org/10.1179/026708309X12468927349370>.
- [55] A.P. Sutton, An analytic model for grain-boundary expansions and cleavage energies, *Philos. Mag. A* 63 (1991) 793–818.
- [56] D. Wolf, Correlation between structure, energy, and ideal cleavage fracture for symmetrical grain boundaries in fcc metals, *J. Mater. Res.* 5 (1990) 1708–1730, [https://doi.org/10.1016/0036-9748\(89\)90482-1](https://doi.org/10.1016/0036-9748(89)90482-1).
- [57] Q. Fan, A new method of calculating interplanar spacing: the position-factor method, *J. Appl. Crystallogr.* 45 (2012) 1303–1308, <https://doi.org/10.1107/S0021889812037764>.
- [58] V. Randle, G.S. Rohrer, Y. Hu, Five-parameter grain boundary analysis of a titanium alloy before and after low-temperature annealing, *Scripta Mater.* 58 (2008) 183–186, <https://doi.org/10.1016/j.scriptamat.2007.09.044>.
- [59] A. Morawiec, On “interface-plane scheme” and symmetric grain boundaries, *Zeitschrift Fur Krist* 227 (2012) 199–206, <https://doi.org/10.1524/zkri.2012.1475>.
- [60] J.K. Mackenzie, J.S. Bowles, The crystallography of martensite transformations—IV body-centred cubic to orthorhombic transformations, *Acta Metall.* 5 (1957) 137–149, [https://doi.org/10.1016/0001-6160\(57\)90018-4](https://doi.org/10.1016/0001-6160(57)90018-4).